



Why is the Pacific meridional mode most pronounced in boreal spring?

Zilu Meng^{1,3} · Tim Li^{1,2}

Received: 20 March 2023 / Accepted: 2 August 2023 / Published online: 21 August 2023
© The Author(s), under exclusive licence to Springer-Verlag GmbH Germany, part of Springer Nature 2023

Abstract

The preferred spring development of the Pacific Meridional Mode (PMM) is investigated through a combined observational analysis and modeling approach. A mixed-layer heat budget analysis shows that the PMM experiences its strongest growth two months prior to its mature phase, and the growth is primarily attributed to the surface latent heat flux (LHF) anomaly, via the wind-evaporation-SST (WES) feedback. The spring-fall difference in the LHF anomaly is caused by both the anomalous and seasonal mean wind fields. Idealized atmospheric general circulation model experiments (GCM) show that given the same PMM heating, atmospheric anomalous wind and LHF responses are much stronger in boreal spring than in boreal fall, which favors a greater WES feedback. Experiments with an intermediate air-sea coupled model with specified SST and surface wind mean state demonstrate that a PMM-like SSTA perturbation grows fastest in boreal spring among all seasons, indicating that the tropical mean wind and SST fields in spring are most favorable for the PMM development. Finally, we show that the atmospheric teleconnection between mid-latitude North Pacific and PMM is much more pronounced during the development of PMM in boreal spring than in boreal fall.

Keywords Pacific meridional mode · Latent heat flux · Seasonal dependence

1 Introduction

A coupled sea surface temperature (SST) and surface wind anomaly pattern over the subtropical northeastern Pacific was defined as the Pacific Meridional Mode (PMM) (Chiang and Vimont 2004). The PMM is characterized by a northeast-southwest tilted SSTA structure and corresponding anomalous southwesterlies or northeasterlies, extending from Baja California all the way to central-western equatorial Pacific. Accompanied with a positive PMM-like SSTA pattern is a low-level cyclonic anomaly to the west, with pronounced low-level southwesterly anomalies being in phase with the tilted positive SSTA. The anomalous southwesterly offsets the mean northeasterly trade wind, leading

to a positive wind-evaporation-SST (WES) feedback (Xie and Philander 1994; Li and Philander 1996). It was shown that the PMM might act as a precursory signal for the formation of an El Niño Southern Oscillation (ENSO) event and a bridge connecting mid-latitude and tropical Pacific (e.g., Alexander et al. 2010).

The PMM may be triggered by perturbations from tropics or mid-latitudes. Previous studies suggested the possible impact of the North Pacific Oscillation (NPO) (Vimont et al. 2009), Aleutian Low (AL) (Chen et al. 2020; Zhang et al. 2022), North Pacific Tripole (NPT) (Zhang et al. 2021), North American Dipole (NAD) (Ding et al. 2019) and North Tropical Atlantic (NTA) (Ham et al. 2013). The common forcing scenario of these modes is that they induce anomalous southwesterlies or northeasterlies in the PMM region. These anomalous winds may further trigger the anomalous SST through the aforementioned positive wind-evaporation-SST feedback.

It has been suggested that the PMM may exert a great impact on ENSO development and initiation (e.g., Amaya 2019). So far two mechanisms were proposed. The first is the seasonal foot-printing mechanism (SFM) (Vimont et al. 2003a; Amaya et al. 2019a). It means that the spring-pronounced positive (negative) PMM can persist until the following summer and the atmospheric response to the PMM SSTA which is

✉ Tim Li
timli@hawaii.edu

¹ Key Laboratory of Meteorological Disaster, Ministry of Education (KLME), Nanjing University of Information Science and Technology, Nanjing, China

² Department of Atmospheric Sciences, University of Hawai'i at Manoa, Honolulu, HI, USA

³ Present Address: Department of Atmospheric Sciences, University of Washington, Seattle, Washington, USA

called summer deep convection (SDC) can induce westerlies (easterlies) at the equator. In the end, it can trigger a positive (negative) ENSO event. The other is a so called trade wind charge (TWC) mechanism (Anderson et al. 2013; Amaya 2019; Chakravorty et al. 2020). The positive PMM can drive southwesterly wind stress anomalies from west-central pacific to north subtropical pacific and easterly wind stress anomalies in east equatorial pacific, leading to a an off-equatorial wind stress curl. This wind stress curl can transport mass equatorward, providing a favorable environment for the development of the positive ENSO event. Therefore, the PMM was considered as a predictor for statistical ENSO prediction (e.g., Lorenzo et al. 2015; Stuecker 2018; Zhang et al. 2009a, b; Zheng et al. 2023). However, PMM-ENSO connection has its own complexity. Recent studies suggested that spring-pronounced PMM has the asymmetric impact on winter ENSO (Zheng et al. 2021a, b). Under the background of the global warming, the PMM's impact on ENSO appears to be enhanced (Jia et al. 2021).

While the PMM pattern may occur in all seasons, its maximum intensity occurs in boreal spring (Wu et al. 2009; Alexander et al. 2010; Vimont 2010; Zhang et al. 2014; Martinez-Villalobos and Vimont 2016, 2017). To understand the season-dependent feature of the PMM, various hypotheses, including the tropical mean state impact (e.g. Vimont et al. 2003b, 2009; Chang et al. 2007; Zhang et al. 2009a, b, 2021; Amaya et al. 2019; Amaya 2019) and the season-dependent mid-latitude forcing (e.g. Vimont et al. 2003b, 2009; Chang et al. 2007; Zhang et al. 2016; Amaya 2019), were suggested, but these hypotheses lacked of solid theoretical and observational approving. The objective of the current study is to conduct a combined theoretical, observational and modeling study to reveal the role of the seas-dependent tropical mean state in the growth rate of the PMM-like perturbation and the effect of the season-dependent mid-latitude forcing on the PMM.

The remaining part of this paper is organized as follows. In Sect. 2, data, models and methods to be used in the current study are briefly described. In Sect. 3 we diagnose the relative roles of mean and anomalous surface winds as well as the sea-air specific humidity differences in modifying surface LHF anomalies during the PMM developing stage. In Sect. 4, we examine the impact of the mean state in affecting the growth of a PMM-like perturbation in a simple coupled atmosphere–ocean model. In Sect. 5, we further analyze the seasonal dependence of North Pacific atmosphere teleconnection during the PMM developing stage. Finally, a conclusion is given in the last section.

2 Data, models and methods

2.1 Data

The observational datasets used in the current study include (1) monthly SST field from the Hadley Centre Global Sea Ice and Sea Surface Temperature (Rayner 2003), (2) monthly 10 m wind, sea level pressure (SLP), surface heat-flux fields from the NCEP-DOE Reanalysis 2 (NCEP2) (Kanamitsu et al. 2002), (3) monthly ocean current, potential temperature and mixed-layer depth fields from NCEP Data Assimilation system (GODAS) (Saha et al. 2006), and (4) Global precipitation data from GPCC (Schneider et al. 2015). All the data above are interpolated to $2^\circ \times 2^\circ$ grid points using linear interpolation. Monthly climatological fields from 1980 to 2018 are subtracted from the original fields to obtain the anomalies.

2.2 Models

2.2.1 An atmospheric GCM

The first model used in the current study is an atmospheric general circulation model (GCM), ECHAM version 4.6 (ECHAM 4.6), which was developed by the Max-Planck Institute for Meteorology (Roeckner et al. 1996). This model is applied to investigate the seasonal dependence of the surface wind and LHF anomaly responses to the same PMM-like heating in boreal spring and fall. The model is run at a $2.8^\circ \times 2.8^\circ$ (T42) horizontal resolution and 19 vertical levels in a hybrid sigma pressure coordinate system. This model was previously used to study atmospheric responses to a specified SSTA or anomalous heating field (e.g., Zhu et al. 2014; Chen et al. 2016; Jiang and Li 2021; Pan et al. 2021a, b).

The horizontal pattern of the specified diabatic heating field is the same as PMM regressed precipitation pattern. Vertically it has an idealized profile with a maximum in middle troposphere, following Pan et al. (2021b). The amplitude of the heating is estimated based on the following equation:

$$\dot{Q} = \frac{pre L_v}{\rho_a C_p H}, \quad (1)$$

where \dot{Q} is the heating rate (unit: K/day), *pre* denotes the precipitation rate (unit: mm/day), $L_v = 2.5 \times 10^6 \text{ J/kg}$ is vaporization latent heat per unit mass, $C_p = 1004 \text{ J} \cdot \text{kg}^{-1} \text{ K}^{-1}$ is the specific heat of the air, $\rho_a = 1004 \text{ J} \cdot \text{kg}^{-1} \text{ K}^{-1}$ is the air density, and $H = 8000 \text{ m}$ denotes the scale height of the atmosphere.

2.2.2 An intermediate coupled atmosphere–ocean model

A Cane-Zebiak type coupled atmosphere–ocean model (Zebiak and Cane 1987) is used. The atmospheric component of the coupled model is a first-baroclinic mode shallow water model (Gill 1980), in which the heating anomaly depends on the perturbation and mean SST. The governing equations of the model are as follows:

$$\epsilon \mathbf{V}'_s + \beta y \mathbf{k} \times \mathbf{V}'_s = -\frac{1}{\rho_a} \nabla p', \tag{2}$$

$$\epsilon_p p' + c_0^2 (\nabla \cdot \mathbf{V}'_s) = -(\alpha T') \exp\left(\frac{(\bar{T} - 30^\circ C)}{16.7^\circ C}\right), \tag{3}$$

where ϵ and ϵ_p are Rayleigh friction and Newtonian damping coefficients, c_0 denotes the first baroclinic mode gravity wave speed, T' and \bar{T} denote anomalous and mean SST, and \mathbf{V}'_s represents the anomalous surface wind. The atmospheric model simulates the anomalous surface wind response to a SSTA forcing under a specified background-mean SST.

The oceanic component includes a reduced gravity shallow water model that describes the changes of ocean thermocline (h) and upper-ocean current (\mathbf{v}), a horizontal momentum equation that describes current shear ($\tilde{\mathbf{v}}$) between the mixed layer and the layer below (Zebiak and Cane 1987), and a mixed-layer temperature (T) equation that predicts the SSTA change caused by 3-dimensional temperature advection and surface latent heat flux anomalies. The governing equations of the oceanic component may be written as:

$$\frac{\partial \mathbf{v}}{\partial t} + f \mathbf{k} \times \mathbf{v} = -g' \nabla h + \frac{\tau}{\rho H} - r \mathbf{v} + \nu \nabla^2 \mathbf{v}, \tag{4}$$

$$\frac{\partial h}{\partial t} + H \nabla \cdot \mathbf{v} = -rh + \kappa \nabla^2 h, \tag{5}$$

$$f \mathbf{k} \times \tilde{\mathbf{v}} = \frac{\tau}{\rho H_1} - r_s \tilde{\mathbf{v}}, \tag{6}$$

$$\begin{aligned} \frac{\partial T}{\partial t} + \mathbf{v}_1 \cdot \nabla (\bar{T} + T) + \bar{\mathbf{v}}_1 \cdot \nabla T \\ = -[M(\bar{w} + w) - M(\bar{w})] \bar{T}_z - M(\bar{w} + w) T_z \\ + \frac{Q}{\rho C_w H_1} - \alpha T + \kappa \nabla^2 T, \end{aligned} \tag{7}$$

$$\mathbf{v}_1 = \mathbf{v} + \frac{H_2}{H} \tilde{\mathbf{v}}, \tag{8}$$

where \mathbf{v}_1 denotes mixed-layer current, w is vertical velocity at the base of the mixed layer determined by the divergence of the mixed-layer current, H and H_1 represent the depth of the average ocean thermocline and oceanic mixed layer, Q denotes the surface heat flux, and τ denotes surface wind stress. All dependent variables with (without) an overbar denote the mean (anomaly) field.

The surface wind stress and latent heat flux anomalies may be written as:

$$\tau = \rho_a C_D V_0 \mathbf{V}'_s, \tag{9}$$

$$Q = Q_{LH} = \rho_a C_D L_c \left[\left| \mathbf{V}'_s + \bar{\mathbf{V}}_s \right| (q_s - q_a) - \left| \bar{\mathbf{V}}_s \right| (\bar{q}_s - \bar{q}_a) \right], \tag{10}$$

where $\rho_a = 10^3 \text{ kg/m}^3$ is the surface air density, $C_p = 4000 \text{ J/kg}$ is the drag coefficient, $\mathbf{V}_s = (u_s, v_s)$ represents horizontal surface wind speed at 10 m, $L_c = 2.5 \times 10^6 \text{ J/kg}$ is vaporization latent heat per unit mass, $q_s(T_s)$ is the saturation specific humidity at SST T_s , q_0 is air specific humidity at 10 m, $\bar{\mathbf{V}}_s$ stands for basic-state surface wind field, and \mathbf{V}'_s represents surface wind anomaly field. A minus sign in the buck formula above indicates that a positive LHF anomaly increases the SSTA. Given the observational fact that the latent heat flux is a primary surface flux component affecting the PMM related SSTA, we consider only the LHF effect in Eq. 7. For details about the simple coupled model, the readers are referred to Li and Philander (1996) and Li (1997b). The background mean state fields are specified from the GODAS dataset.

2.3 Methods

2.3.1 Mixed layer heat budget analysis

To understand the role of ocean dynamics processes and surface heat fluxes in causing the PMM development, an ocean mixed layer heat budget analysis (Chen et al. 2016, 2021; Jiang and Li 2019, 2021; Chen and Li 2021) was performed. The mixed layer temperature anomaly (MLTA) tendency equation may be written as:

$$\frac{\partial T'}{\partial t} = -(\tilde{\mathbf{V}} \cdot \nabla T)' + \frac{Q'_{net}}{\rho C_p H} + R, \tag{11}$$

$$Q_{net} = Q_{LHF} + Q_{SW} + Q_{LW} + Q_{SHF} \tag{12}$$

where T represents the mixed layer temperature; $\bar{\mathbf{V}}$ represents three-dimensional (3D) ocean current; the first term in the right-hand side of Eq. (11) represents the 3D temperature advection, $\bar{\mathbf{V}} \cdot \nabla T = u \frac{\partial T}{\partial x} + v \frac{\partial T}{\partial y} + w \frac{\partial T}{\partial z}$. Recent studies sug-

gested that term $w \frac{\partial T}{\partial z}$ should be replaced by $\left(\frac{\partial h}{\partial t} + w_{-h} + u_{-h} \frac{\partial h}{\partial x} + v_{-h} \frac{\partial h}{\partial y}\right) \frac{T-T_{-h}}{h}$ in which h represents the mixed layer depth to explicitly describe the entrainment at the base of the mixed layer (Vijith et al. 2020; Cheng et al. 2022). However, our calculation shows that the difference of the 3D temperature advection is small (less than 3%). Q_{net} denotes the net ocean surface heat flux containing surface latent heat flux (Q_{LHF}), sensible heat flux (Q_{SHF}), shortwave radiation (Q_{SW}) and longwave radiation (Q_{LW}); $\rho = 10^3 \text{ kg/m}^3$ is the density of water, $C_p = 4000 \text{ J/kg}$ is the specific heat of water, and H denotes the monthly mean ocean mixed layer depth. The mixed layer heat budget analysis was estimated based on the GODAS and NCEP2 datasets.

2.3.2 Decomposition of surface latent heat flux anomalies

To reveal the relative roles of anomalous wind speed and anomalous air-sea specific humidity difference in causing the LHF anomaly, we use Taylor Expansion to simplify the Eq. (10) to:

$$Q'_{LHF} = -\rho_a C_D L_v \left(|\mathbf{V}_s|' (\bar{q}_s - \bar{q}_a) + |\bar{\mathbf{V}}_s| (q_s - q_a)' + |\mathbf{V}_s|' (q_s - q_a)' + R \right) \quad (13)$$

where $C_D = 1.4 \times 10^{-3}$ is the drag coefficient. The first term in the right-hand side of Eq. (13) (term1) represents the LHF anomaly caused by the wind anomaly, and $|\mathbf{V}_s|' = \frac{\mathbf{V}_s' \cdot \bar{\mathbf{V}}_s}{|\bar{\mathbf{V}}_s|}$ which is derived using Taylor's first order expansion is used in calculation. The second term (term2) denotes the contribution from the air-sea specific humidity difference anomaly. The third term (term3) represents the nonlinear contribution of the anomalous wind and air-sea specific humidity difference fields. In the tropics, the second term in general is a damping term as the anomalous air-sea specific humidity difference is proportional to the underlying SST anomaly (Li and Philander 1996; Li 1997b). Thus, the most efficient way to heat the ocean surface is through the reduction of the surface wind speed when the anomalous wind vector is against the mean wind vector.

3 Factors causing the phase locking of PMM: An observational analysis.

An Empirical Orthogonal Function (EOF) analysis (Cheng et al. 1995) of the monthly SSTA field in the tropical Pacific (20°S–30°N, 150°E–85°W) during 1980–2018 was conducted to reveal the spatial patterns and time evolution of dominant modes. As expected, the first EOF mode is

characterized by a pronounced ENSO structure, with the largest SSTA in the equatorial eastern Pacific (Fig. 1a). This mode explains 53.4% of total variance. The second mode exhibits a PMM-like structure, with a maximum SSTA elongated from northeastern tropical Pacific to equatorial western Pacific (Fig. 1b). The second mode explains 13.2% of total variance. Associated anomalous wind fields were derived by regressing the surface wind field onto the principal components (PCs) of the two leading EOF modes (shown in Fig. 1c).

There are two other methods to define PMM. A traditional method to obtain the leading patterns is through the Maximum Covariance Analysis (MCA) of both the anomalous SST and wind fields in the tropical Pacific (20°S–30°N, 150°E–85°W) (Chiang and Vimont 2004). A recent study defined the PMM index as the regional average SSTA over 5°N–25°N, 160°W–120°W after regressing out the cold tongue index (CTI, SSTA averaged over 180°–90°W, 6°S–6°N) (Richter et al. 2022). The results from the two methods are quite similar to that shown in Fig. 1b. The temporal and spatial correlations between the EOF-based PMM and the two methods exceed 0.9 and pass the confidence level of 99.9% using

the student-*t* test (seeing Supplementary Figs. 1 and 2). It is worth mentioning that some previous studies defined the second EOF mode of the tropical Pacific SSTA as El Niño Modoki (Ashok et al. 2007). A caution is needed to interpret the El Niño Modoki as the PMM, because the former has a peak phase in northern winter, while the PMM has a peak season in northern spring. There is also a debate regarding how to define the central Pacific El Niño events (Xiang et al. 2013).

To reveal the season-dependent intensity of PMM, an off-equatorial (beyond 5°N) region (green box shown in Fig. 1b), named the key PMM region (KPR), is selected based on the criterion of the SSTA in Fig. 1b being greater than 0.17 K. Therefore, KPR makes our research focus on the SSTA mode that tilts northeast-southwest and is outside the equator. The time correlation between KPR-averaged SSTA and PMM PC is 0.74 meaning that the KPR region explains most variability of the PMM. In fact, the KPR keeps almost unchanged with different PMM definitions and the selection criteria for KPR SSTA will not change the conclusions of our subsequent observation analysis (Seeing Supplementary Table 1 and Supplementary Fig. 1).

To inspect the seasonal intensity, Fig. 1d shows the variances of the two leading modes at each season. While the ENSO mode is strongest in boreal winter (DJF), the

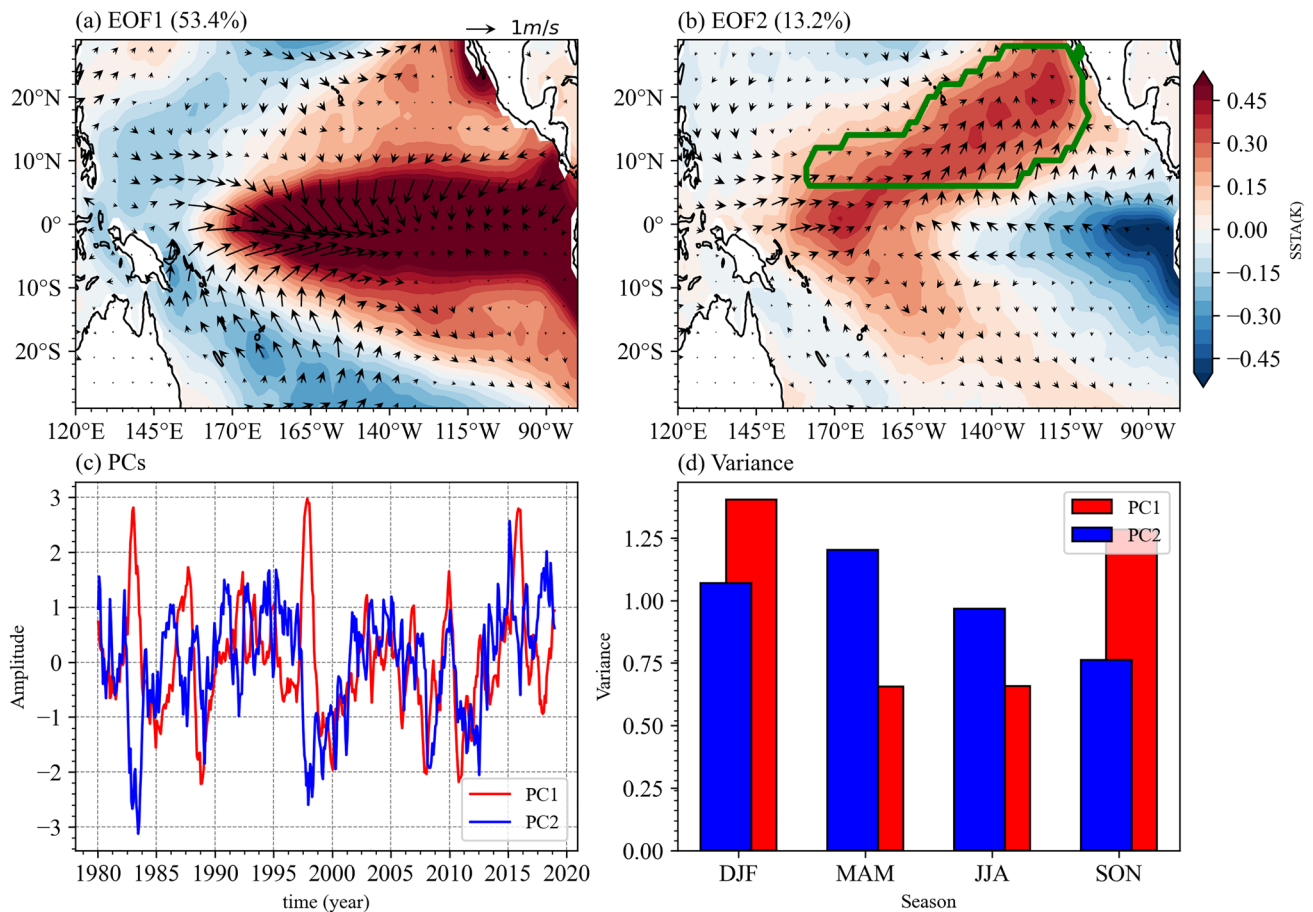


Fig. 1 The result of the EOF method. Regression of the the first and second EOF patterns (a–b) of the SSTA (shaded, unit: °C) in the tropical Pacific during 1980–2018, and green box in (b) outlines the PMM key region (KPR), where SSTA is larger than 0.17 K and loca-

tion is North of 5°N. Vectors are 10 m wind anomaly fields regressed onto PC1 and PC2. (c) Normalized PC1 and PC2. (d) Variance of the two leading EOF modes as a function of season

PMM retains the greatest strength in boreal spring (MAM) and is weakest in boreal autumn (SON). It has been shown that the ENSO phase locking is likely attributed to a season-dependent coupled instability (Li 1997a; Chen and Jin 2020) and anomalous wind forcing in western Pacific associated with the development of a Philippine-Sea anomalous anticyclone (Wang et al. 2000, 2003). The cause of the phase locking of PMM, however, remains elusive.

To understand the phase locking of the PMM, we first analyze the time evolution of PMM and associated SSTA tendency for all seasons. Figure 2a shows that the area-averaged SSTA over the KPR has the fastest growth rate 2 months prior to the PMM peak, which can be regarded as the PMM developing phase. A mixed-layer ocean heat budget analysis during the developing phase was further carried out in the region. The diagnosis result indicates that the thermodynamic (i.e., surface heat flux) term, particularly the surface LHF component, played the main role in the development of the PMM SSTA in the KPR. The

sensible heat flux (SHF) also plays a role, but much less vital compared to the LHF term, as shown in Fig. 2b. The diagnosed MLTA tendency is quite close to the observed SSTA tendency, adding the confidence of the mixed-layer heat budget analysis result.

Given the dominant role of the surface LHF anomaly in contributing the PMM tendency, we next investigate the difference of the observed LHF anomaly in two extreme seasons, boreal spring (March–April–May, MAM) and boreal autumn (September–October–November, SON). Because of the two-month difference between the peak phases of the SSTA and its tendency, the LHF analysis for boreal spring (fall) is confined to January–February–March (July–August–September).

Figure 3a shows the diagnosed result of the decomposed LHF terms for boreal spring and fall. As seen in Fig. 3a, term1 is a dominant term for both the spring and fall seasons. There is a marked difference in the LHF anomaly

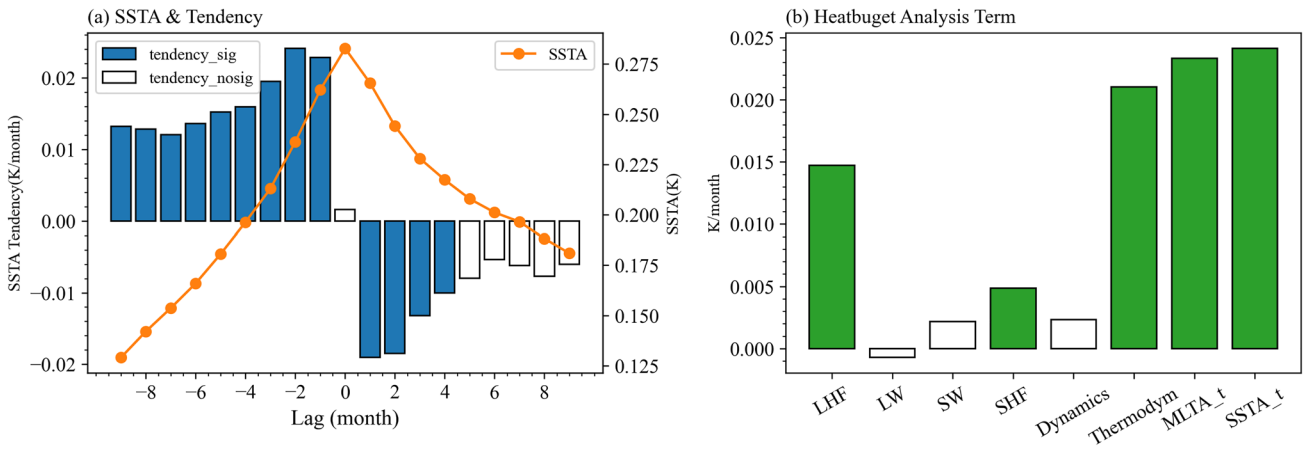


Fig. 2 **a** The KPR mean SSTA (orange line, right y-axis) and SSTA tendency (bar, left y-axis) regressed on PMM PC. All the SSTA is above 95% confidence level; the bars filled with blue (white) denotes above (below) 95% confidence level. **b** The KPR mean mixed layer heat budget analysis term (bar) regressed on 2-month lag PMM PC.

The bars filled with green (white) denotes above (below) 95% confidence level. The “Thermodym” means thermal dynamics term, “MLTA_t” means MLTA tendency and “SSTA_t” means SSTA tendency

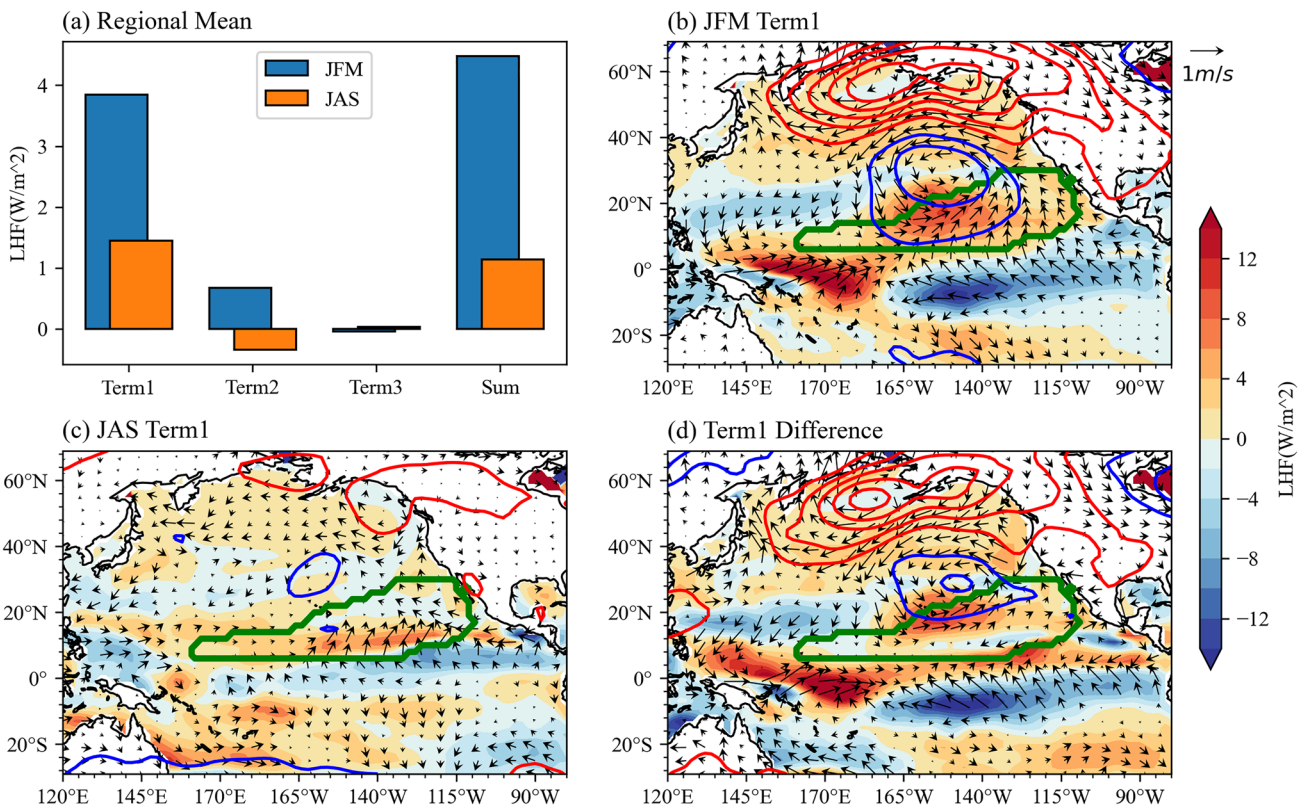


Fig. 3 The result of Linearized LHF anomaly analysis. **a** The KPR average LHF anomaly three terms and summary in the JFM and JAS. **b–c** Shadings are JFM and JAS’s LHF anomaly term1 spatial pattern. Quivers are 10 m wind anomalies in JFM and JAS regressed on

MAM and SON PMM PC. Contour is SLP anomaly in JFM and JAS regressed on MAM and SON PMM PC. (Contour interval: 0.4 hPa; red for positive and blue for negative). The difference between (b) and (c) are show in (d)

between boreal spring and fall. Such a difference is critical in generating the PMM season-dependence.

The LHF term1 difference depends on both the anomalous wind and the mean wind fields in the two corresponding

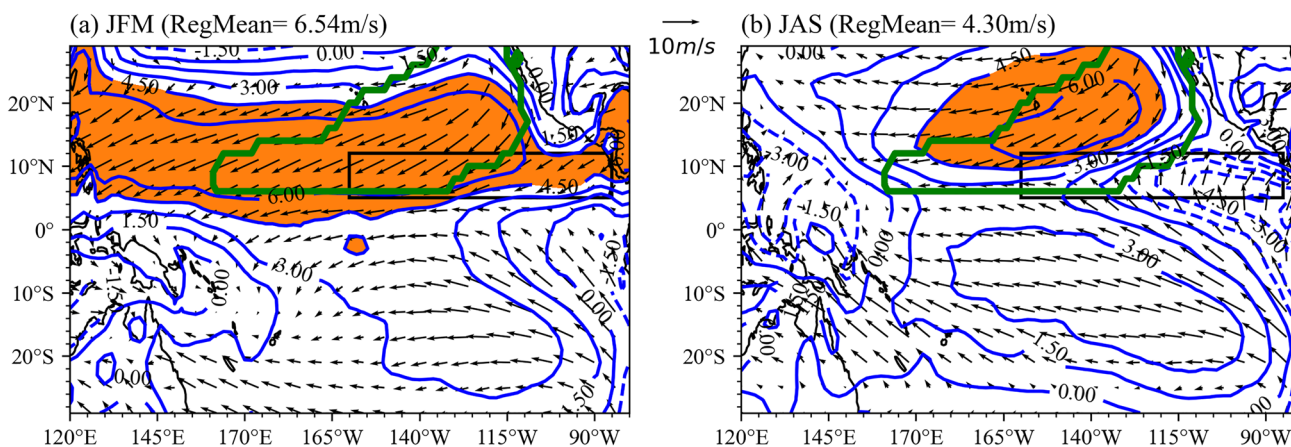


Fig. 4 Climatological mean 10 m wind fields (vectors) in JFM (a) and JAS (b). Contour shows the mean northeast component of the wind at 10 m, meaning $(-\frac{1}{\sqrt{2}}u - \frac{1}{\sqrt{2}}v)$. Orange shading denotes the region where the northeast component exceeds 4.5 ms^{-1} in the north-

easterly trade zone. The black box denotes a contrasting region between pronounced northward cross-equatorial flow in JAS and southward retreat of the cross-equatorial flow in JFM. And KPR mean northeast wind speed is 6.54 m/s (4.30 m/s) in JFM (JAS)

seasons. Figure 3b and c illustrate the horizontal patterns of the surface wind anomaly and the term1 LHF fields for the two seasons. Note that southwesterly anomalies occupy nearly the whole KPR in the spring season (Fig. 3b). The wind anomalies offset the mean northeasterlies, reducing the more LHF transported by the ocean to the atmosphere, meaning heating the ocean, leading to warmer SSTA over KPR. On the contrary, in the fall season, southwesterly anomalies occupy only a small area of the KPR, reducing less LHF from ocean to atmosphere and getting less warm SSTA in KPR (Fig. 3c). The difference map (Fig. 3d) indicates clearly that the anomalous wind speed induced LHF field plays a critical role in generating the preferred development of PMM in boreal spring.

It is worth mentioning that the term1 difference is contributed by both the anomalous wind and the seasonal mean wind differences between the two seasons. Figure 4 illustrates the mean surface wind fields in JFM and JAS. Northeasterly mean trade winds are much stronger and more pronounced in JFM than in JAS. In boreal spring, the equatorial cold tongue is weakest (Li and Philander 1996; Philander et al. 1996), which leads to the weakest cross equatorial flow and southernmost location for the ITCZ. As a result, strong northeasterly trade winds cover the most of tropical North

Pacific (Fig. 4a). This allows most efficient WES feedback north of the equator. In contrast, the equatorial cold tongue is strongest in boreal fall, and as a result, the ITCZ shifts northward, and the northeasterly trades cover a smaller area. This leads to a less efficient WES feedback over the KPR.

The argument above implies the importance of the mean wind in generating the anomalous LHF, that is, even given the same anomalous wind field, a greater LHF anomaly would be generated in association with boreal spring PMM due to the seasonal difference in the mean wind field. On the other hand, Fig. 3b–c show clearly that there is a marked difference in the anomalous surface wind fields. In JFM, the PMM anomalous wind is closely linked to a North Pacific Oscillation (NPO) like patterns (Rogers 1981) in mid-latitude North Pacific, whereas in JAS the anomalous wind is primarily linked to equatorial SSTA and its link to mid-latitude North Pacific is weak. This observational result motivates us to further examine the cause of the anomalous wind patterns associated with PMM during the two extreme seasons.

Idealized numerical model experiments were further carried out to elucidate the role of the mean state in affecting the anomalous wind response to PMM. Two sets of ECHAM model experiments are designed. As shown in

Table 1 List of numerical experiments with ECHAM4.6

Experiments	Description
CTRL	Forced by global climatological monthly SST field
EXP_PMM	Forced by the global climatological SST and a PMM-like diabatic heating anomaly over the tropical Pacific (30°N–30°S, 120°E–90°W)

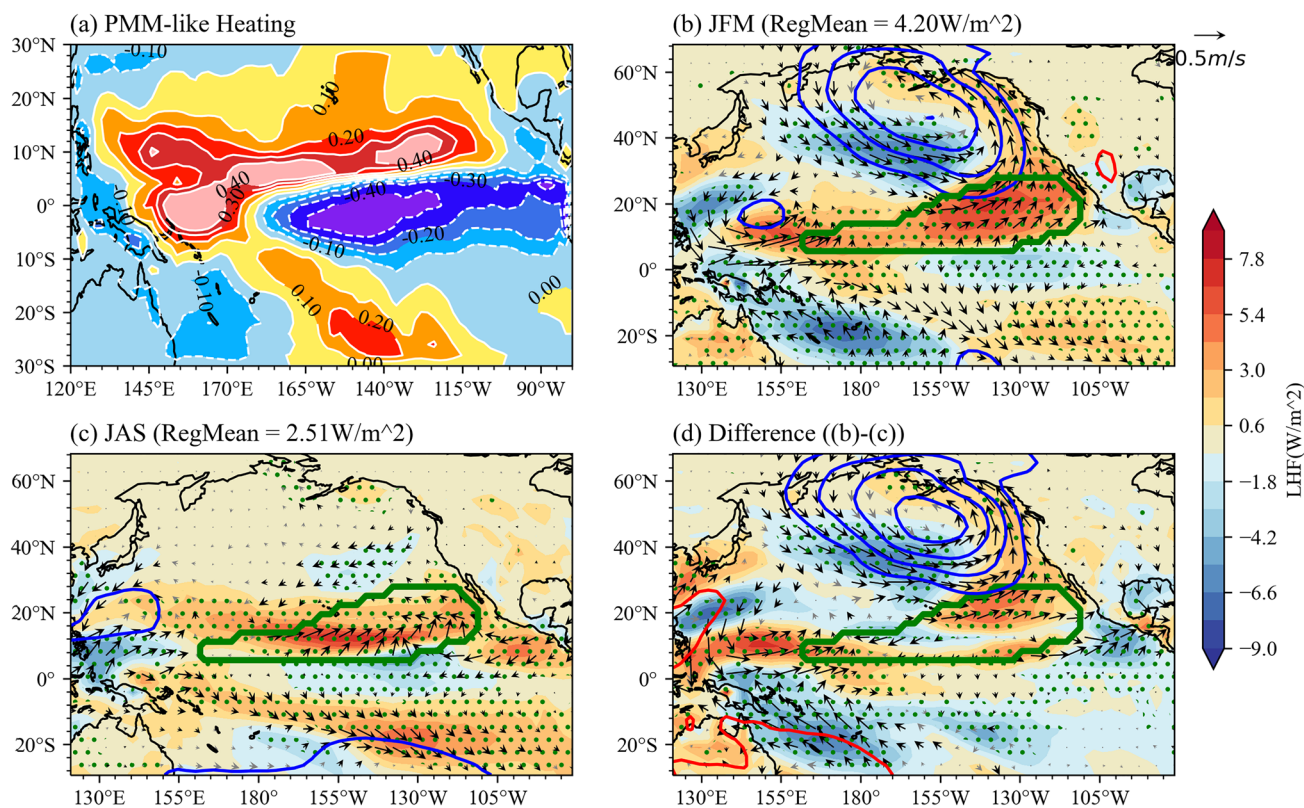


Fig. 5 The PMM-like heating (a) added to ECHAM model and experiment results in JFM (b) and JAS (c). In (b) and (c), vectors denote 10 m wind anomaly (black (grey) vector is above (below) 95% confidence level), contour are SLP anomalies. (Contour inter-

val: 0.4 hPa; red for positive and blue for negative), and shadings are LHF anomalies and green dots show the LHF anomaly values passing the confidence level of 95% using the student-t test. (d) the difference between (b) and (c) is shown

Table 1, in the control experiment, the model is integrated for 30 years with prescribed observed climatological SST field derived from the HadISST dataset. In the sensitivity experiment (EXP_PMM), a PMM-like diabatic heating, which is derived from PMM regressed precipitation pattern (shown in Fig. 5a), was specified. By subtracting the control experiment from the sensitivity simulation results, one may examine the anomalous atmospheric response to the same PMM forcing in different seasons under different mean states.

Figure 5b–c shows the anomalous wind, LHF and SLP responses in JFM and JAS. Same as the observed, the anomalous wind associated with PMM may extends to the mid-latitude North Pacific in JFM, whereas it is confined in the tropics in JAS. The atmospheric modeling result implies that the tropical-mid-latitude teleconnection is much more active during JFM than during JAS. Because of the season-dependent teleconnection feature, the anomalous wind and associated LHF anomaly are most pronounced in the whole PMM regions in JFM, whereas they are only confined to the southern PMM region. The season-dependent anomalous wind response is better seen in the difference map (Fig. 5d). The difference in the anomalous wind response leads to distinct

LHF anomaly patterns and thus distinct PMM SSTA growth rates, contributing to the seasonal dependence of the PMM.

It is worth mentioning that there is a marked difference in the mid-latitude circulation between Figs. 3b and 5b. This implies that the NPO-like pattern in North Pacific shown in Fig. 3b is not a direct response to the PMM heating, rather it might be a precursory condition for the generation of PMM. The simulated SLP field over North Pacific (Fig. 5b), to a certain extent, resembles the AL pattern. Recent studies showed that this pattern plays an important role in the PMM-ENSO cycle (Zhang et al. 2022), and is responsible for recent increased emergence of the central Pacific ENSO (Chen et al. 2023). We will further explore the relationship between the North Pacific atmospheric circulation and the development of the PMM in Sect. 5.

4 Season-dependent growth rates of a PMM-like perturbation in a simple coupled model

In this section, we aim to demonstrate that the boreal spring season is the season when PMM develops fastest using an intermediate coupled atmosphere–ocean model, a

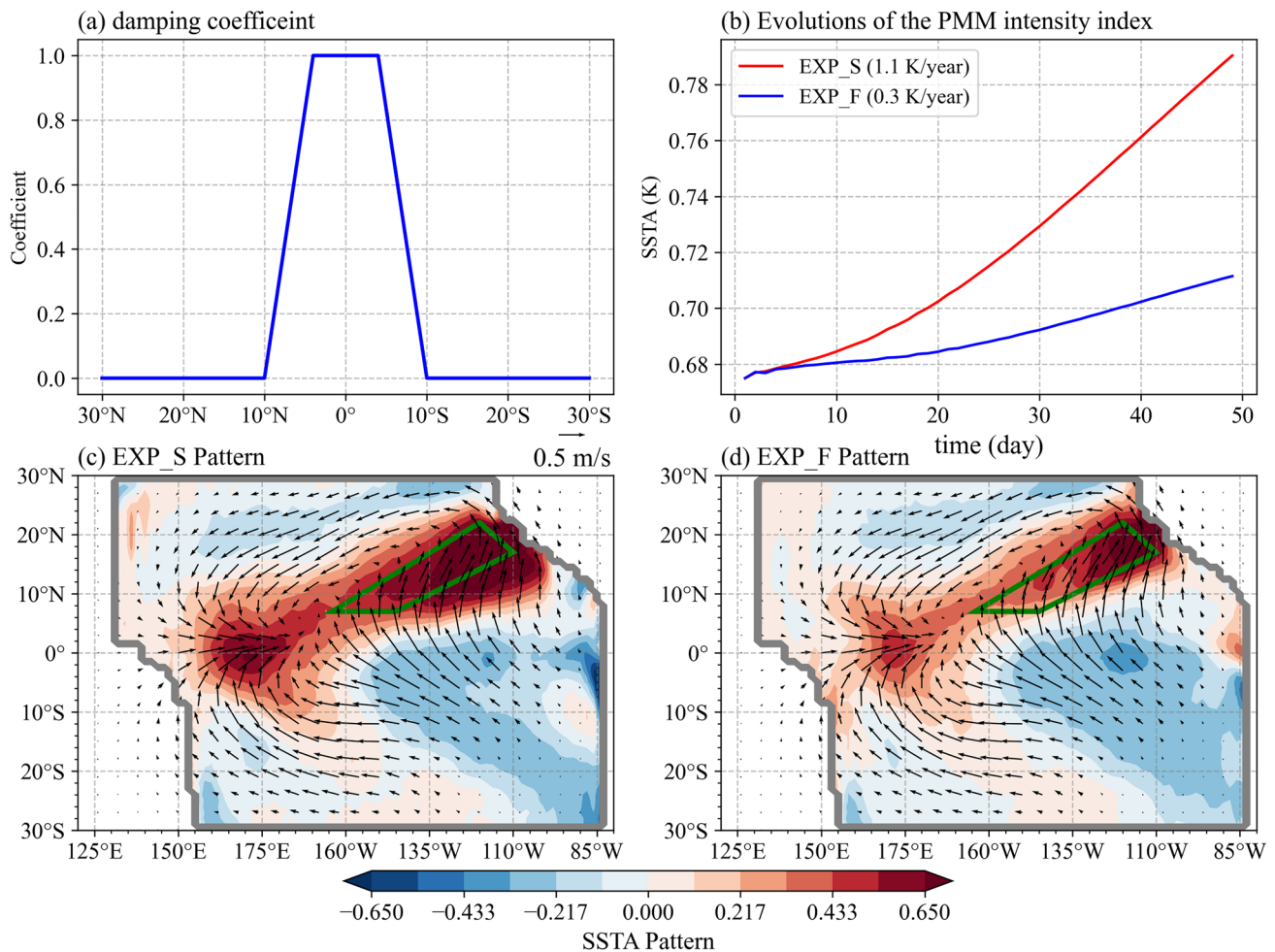


Fig. 6 The damping coefficients, pattern and strength of the experiments. **a** The meridional distribution of a thermal damping coefficient in the SSTA equation with latitude. **b** Evolutions of the PMM intensity index in EXP_S (solid red), EXP_F. **c–d** The anomalous SST

and wind patterns of the most unstable mode in the simple coupled model, averaged during the first 30 days, in EXP_S (c) and EXP_F (d). The green quadrilateral box is used to calculate the PMM intensity index

Cane-Zebiak type model described in Sect. 2. To focus on the perturbation development in the off-equatorial region, we intentionally suppress the ENSO mode by applying a strong thermal damping (with a revised time scale of 60 days) in the equatorial zone (4°N and 4°S). Figure 6a shows the latitudinal distribution of this thermal damping. The damping coefficient is a constant in the equatorial zone and decreases linearly to zero at 10°N and 10°S. Two parallel experiments, namely EXP_S and EXP_F, are designed to investigate the growth of a specified initial weak SSTA perturbation that has the same pattern as in Fig. 1b but with a smaller amplitude (0.8 times of Fig. 1b values) and different amplitudes don't influence experimental results (seeing Supplementary Table 2). In EXP_S, the mean state condition in JFM is specified as a background basic state. In EXP_F, the JAS mean state condition is specified.

As expected, the initial PMM-like perturbation grows in both the season through the WES feedback. Figure 6b shows the time evolution of the area-averaged SSTA in the PMM region from the two experiments, while Fig. 6c and d illustrate unstable mode patterns averaged during the initial 30 days. Note that in the bottom panel both the SST and wind anomaly fields have been normalized so that one can see clearly their horizontal patterns. As seen from Fig. 6c and d, the most unstable mode in both the experiments illustrates a northeast-southwest tilted SSTA pattern similar to the observed. A low-level cyclonic circulation anomaly appears to the northwest of the tilted warm SSTA zone, as a Rossby wave response to the SSTA forcing.

The time evolutions of the area-averaged PMM SSTA intensity show an exponential growth characteristic, with a much stronger growth in the boreal spring season. One may estimate the PMM growth rate based on the time

evolution curves, say, from day 5 to day 30, using the least squares method. Our calculation shows that the growth rate is 1.1 year^{-1} in EXP_S and in 0.3 year^{-1} EXP_F. Additional experiments with the boreal winter and summer mean-state conditions were carried out, and the result indicates that their growth rates are somewhere between EXP_S and EXP_F. Therefore, the intermediate coupled model experiments demonstrate that the PMM grows fastest and thus is most pronounced under the boreal spring mean state condition. The result implies that the tropical mean state, in particular the mean wind field, is critical in generating the season-dependent PMM feature.

5 Possible effects of extratropical atmospheric forcing in PMM season preference

In addition to the tropical mean state, extratropical atmospheric forcing may also play a role in contributing to the seasonal preference of PMM. It has been shown in Sect. 3 from both the observational analysis and AGCM experiments that PMM appears more linked to mid-latitude North Pacific atmosphere in boreal spring than in boreal fall. The previous study suggested that NPO may trigger PMM development

(e.g. Chang et al. 2007; Vimont et al. 2009; Zhang et al. 2022). This motivates us to further explore the impact of signals outside the tropics on the development of PMM.

The EOF analysis of the SLP anomaly field in the North Pacific domain (10°N – 55°N , 130°E – 110°W) was carried out to reveal the spatial patterns and time evolutions of the two leading modes. The first mode is characterized by a low-pressure center near Aleutian Islands (hereafter the AL mode, Pickart et al. 2009) (Fig. 7a). It explains 43.1% of total variance. The southeasterly anomalies to the southeast corner of the AL mode are overlapped with northern PMM region, and thus they may be conducive to the development of PMM. The second mode is characterized by a north–south dipole pattern (Rogers 1981; Yeh and Kirtman 2004; Park et al. 2013; Chen and Wu 2018) and is named as the NPO mode (Fig. 7b). It explains 15.2% of total variance. The low pressure anomaly associated with the NPO mode may induce strong southwesterlies in the subtropical PMM region, triggering the development of PMM.

A lagged (2-month) correlation analysis with the PMM time series indicates that both the AL and NPO modes are significantly correlated with PMM in boreal spring and such lagged correlations are much weaker in boreal fall (Fig. 7c). This indicates that there are significant atmospheric

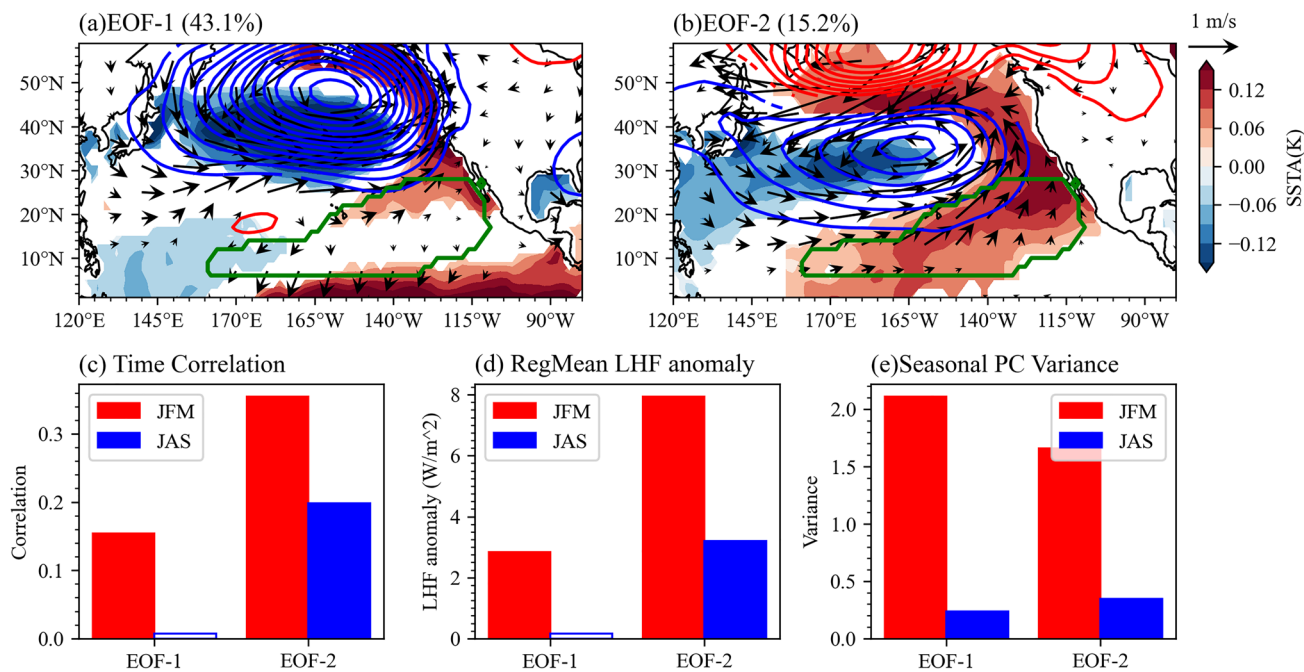


Fig. 7 The result of the EOF method on SLP anomaly (10°N – 55°N , 130°E – 110°W). The first and second EOF patterns (a–b) of the SLP anomalies (contour interval: 0.4 hPa, red for positive and blue for negative) during 1980–2018, and green box in (a) and (b) denotes KPR (the same as Fig. 1(b)). Vectors are 10 m wind anomaly fields regressed onto PC1 and PC2. Shadings are 2-month lag SSTA

regressed on EOF PCs. All plotted values passed the 95% confidence t-test. **c** The correlation between EOF PCs and 2-month lag PMM PC **(d)** Regress KPR area-averaged LHF anomaly on simultaneous EOF PCs. **e** Variance of the two leading EOF modes as a function of season. Filled bars in (c)–(e) mean values pass the 95% confidence test and red for the JFM and blue for the JAS

precursory signals in North Pacific during the PMM development stage.

The impact of the mid-latitude North Pacific modes (i.e., the AL and NPO modes) on PMM may further be inferred from the regressed LHF anomaly shown in Fig. 7d. Note that the area-averaged LHF anomalies over the KPR regressed to the AL and NPO modes are much greater and statistically more significant in boreal spring than in boreal fall (Fig. 7d). Such the season-dependent forcing characteristic may be further validated from the strength of the two mid-latitude modes (Fig. 7e). Both the AL and NPO modes have much greater variances and are much more pronounced in boreal spring than in boreal fall.

To sum up, significant atmospheric precursory signals appear in North Pacific in boreal spring prior to the PMM development and such signals are much weaker and insignificant in boreal fall. The mid-latitude signals in boreal spring may trigger the development of PMM through induced anomalous wind in subtropics. Therefore, the mid-latitude forcing may provide an additional mechanism for the PMM seasonal preference.

6 Conclusion

In this study we investigate the physical mechanism responsible for the PMM preference in boreal spring through a combined observational and modeling study. In the observational analysis, we conducted a mixed-layer heat budget diagnosis, and revealed that the LHF anomaly is a dominant term affecting the PMM SSTA development. A further decomposition of the LHF term shows that the wind speed related component plays a dominant role while the air-sea specific humidity difference related contribution is much weaker. The seasonal difference of the LHF anomaly over the PMM region between boreal spring and fall arises from both the anomalous and mean wind fields. The mean wind effect on the LHF anomaly is further demonstrated with idealized AGCM experiments in which the same PMM heating anomaly is specified.

An intermediate coupled atmosphere–ocean model is further utilized to investigate the season-dependent growth of the PMM perturbation. Two idealized numerical experiments are designed, in which the background mean wind and SST fields are specified from the boreal spring and fall conditions. Initially a PMM-like SSTA perturbation with a moderate amplitude is specified. The numerical experiments demonstrate clearly that PMM is the most unstable mode in the off-equatorial region and that the strongest growth of the PMM perturbation occurs in boreal spring. This points out the important role of the tropical mean state in controlling the seasonal preference of PMM.

The possible role of the mid-latitude North Pacific atmospheric forcing in affecting the seasonal dependence of PMM is further explored. Two dominant atmospheric (AL and NPO) models in North Pacific were found, and they are significantly correlated with PMM at a two-month lead in boreal spring but much less so in boreal fall. The result implies an additional mid-latitude forcing mechanism in the PMM phase-locking.

It is worth mentioning that a simple coupled model is used in the current study to reveal the mean state effect. While the simple model has an advantage to separate the anomaly and mean fields, it involves various assumptions. For example, a constant oceanic mixed layer is assumed in the current framework, and only surface latent heat flux is considered in the surface heat flux term. The atmospheric heating in the model is simply proportional to the underlying SSTA. A further study with a more sophisticated coupled atmosphere–ocean model is needed to test the season-dependent characteristic of PMM and to confirm the current simple model results.

The effect of ENSO on the seasonal dependence of PMM remains an open question. Some studies have indicated that the seasonal variance and dependence of PMM do not change after removing the influence of ENSO in a coupled GCM (Zhang et al. 2021). However, this does not imply that ENSO has no impact on PMM seasonal dependence. For instance, DJF-pronounced ENSO generates an AL-like pattern, which is a Pacific North American (PNA) pattern (Wallace and Gutzler 1981) at high levels, leading to PMM development in the following year's JFMAM season (as shown in Sect. 5; Zhang et al. 2022). Therefore, further research is necessary to understand the role of ENSO in PMM phase-locking.

Supplementary Information The online version contains supplementary material available at <https://doi.org/10.1007/s00382-023-06914-4>.

Acknowledgements This work was supported by National Natural Science Foundation of China (NSFC) grant 42088101 and National Science Foundation (NSF) grant AGS-2006553. Z.M. would like to thank Professor Lin Chen, Dr. Ming Sun, Dr. Xiaohui Wang, Dr. Xiao Pan, and Dr. Leishan Jiang at Nanjing University of Information Science and Technology for their invaluable advice and help in learning and running the numerical model.

Funding This work was supported by National Natural Science Foundation of China (NSFC) grant 42088101 and National Science Foundation (NSF) grant AGS-2006553.

Data Availability The Hadley Centre Sea Ice and Sea Surface Temperature data sets are publicly available at: <https://www.metoffice.gov.uk/hadobs/hadisst/>. The NCEP2 datasets are publicly available at: <https://psl.noaa.gov/data/gridded/data.ncep.reanalysis2.html>. The GODAS datasets are available at <https://psl.noaa.gov/data/gridded/data.godas.html>. The GPCP data are available at <https://psl.noaa.gov/data/gridded/data.gpcp.html>.

Declarations

Conflict of interest All authors declare no conflict of interest.

References

- Alexander MA, Vimont DJ, Chang P, Scott JD (2010) The impact of extratropical atmospheric variability on ENSO: testing the seasonal footprinting mechanism using coupled model experiments. *J Clim* 23:2885–2901. <https://doi.org/10.1175/2010JCLI3205.1>
- Amaya DJ (2019) The Pacific meridional mode and ENSO: a review. *Curr Clim Change Rep* 5:296–307. <https://doi.org/10.1007/s40641-019-00142-x>
- Amaya DJ, Kosaka Y, Zhou W et al (2019) The North Pacific pace-maker effect on historical ENSO and its mechanisms. *J Clim* 32:7643–7661. <https://doi.org/10.1175/JCLI-D-19-0040.1>
- Anderson BT, Perez RC, Karspeck A (2013) Triggering of El Niño onset through trade wind-induced charging of the equatorial Pacific: trade wind charging of the EQ. *Pacific Geophys Res Lett* 40:1212–1216. <https://doi.org/10.1002/grl.52000>
- Ashok K, Behera SK, Rao SA et al (2007) El Niño Modoki and its possible teleconnection. *J Geophys Res* 112:C11007. <https://doi.org/10.1029/2006JC003798>
- Chakravorty S, Perez RC, Anderson BT et al (2020) Testing the trade wind charging mechanism and its influence on ENSO variability. *J Clim* 33:7391–7411. <https://doi.org/10.1175/JCLI-D-19-0727.1>
- Chang P, Zhang L, Saravanan R et al (2007) Pacific meridional mode and El Niño—Southern Oscillation. *Geophys Res Lett.* <https://doi.org/10.1029/2007GL030302>
- Chen H-C, Jin F-F (2020) Fundamental behavior of ENSO phase locking. *J Clim* 33:1953–1968. <https://doi.org/10.1175/JCLI-D-19-0264.1>
- Chen M, Li T (2021) ENSO evolution asymmetry: EP versus CP El Niño. *Clim Dyn* 56:3569–3579. <https://doi.org/10.1007/s00382-021-05654-7>
- Chen S, Wu R (2018) Impacts of winter NPO on subsequent winter ENSO: sensitivity to the definition of NPO index. *Clim Dyn* 50:375–389. <https://doi.org/10.1007/s00382-017-3615-z>
- Chen L, Li T, Behera SK, Doi T (2016) Distinctive precursory air-sea signals between regular and super El Niños. *Adv Atmos Sci* 33:996–1004. <https://doi.org/10.1007/s00376-016-5250-8>
- Chen S, Chen W, Wu R et al (2020) Potential impact of preceding aleutian low variation on El Niño-Southern oscillation during the following winter. *J Clim* 33:3061–3077. <https://doi.org/10.1175/JCLI-D-19-0717.1>
- Chen M, Yu J-Y, Wang X, Chen S (2021) Distinct onset mechanisms of two subtypes of CP El Niño and their changes in future warming. *Geophys Res Lett.* <https://doi.org/10.1029/2021GL093707>
- Chen S, Chen W, Yu B et al (2023) Enhanced impact of the Aleutian low on increasing the central pacific ENSO in recent decades. *NPJ Clim Atmos Sci* 6:1–13. <https://doi.org/10.1038/s41612-023-00350-1>
- Cheng X, Nitsche G, Wallace JM (1995) Robustness of low-frequency circulation patterns derived from EOF and rotated EOF analyses. *J Climate* 8:1709–1713. [https://doi.org/10.1175/1520-0442\(1995\)008%3c1709:ROLFCP%3e2.0.CO;2](https://doi.org/10.1175/1520-0442(1995)008%3c1709:ROLFCP%3e2.0.CO;2)
- Cheng X, Chen S, Chen W, Hu P (2022) Observed impact of the Arctic oscillation in boreal spring on the Indian Ocean dipole in the following autumn and possible physical processes. *Clim Dyn.* <https://doi.org/10.1007/s00382-022-06616-3>
- Chiang JCH, Vimont DJ (2004) Analogous pacific and atlantic meridional modes of tropical atmosphere-ocean variability. *J Clim* 17:4143–4158. <https://doi.org/10.1175/JCLI4953.1>
- Ding R, Li J, Tseng Y et al (2019) Linking the North American dipole to the pacific meridional mode. *J Geophys Res Atmos* 124:3020–3034. <https://doi.org/10.1029/2018JD029692>
- Gill AE (1980) Some simple solutions for heat-induced tropical circulation. *QJ Royal Met Soc* 106:447–462. <https://doi.org/10.1002/qj.49710644905>
- Ham Y-G, Kug J-S, Park J-Y, Jin F-F (2013) Sea surface temperature in the north tropical Atlantic as a trigger for El Niño/Southern oscillation events. *Nat Geosci* 6:112–116. <https://doi.org/10.1038/ngeo1686>
- Jia F, Cai W, Gan B et al (2021) Enhanced North Pacific impact on El Niño/Southern oscillation under greenhouse warming. *Nat Clim Chang* 11:840–847. <https://doi.org/10.1038/s41558-021-01139-x>
- Jiang L, Li T (2019) Relative roles of El Niño-induced extratropical and tropical forcing in generating Tropical North Atlantic (TNA) SST anomaly. *Clim Dyn* 53:3791–3804. <https://doi.org/10.1007/s00382-019-04748-7>
- Jiang L, Li T (2021) Impacts of Tropical North Atlantic and Equatorial Atlantic SST anomalies on ENSO. *J Clim* 34:5635–5655. <https://doi.org/10.1175/JCLI-D-20-0835.1>
- Kanamitsu M, Ebisuzaki W, Woollen J et al (2002) NCEP–DOE AMIP-II Reanalysis (R-2). *Bull Amer Meteor Soc* 83:1631–1644. <https://doi.org/10.1175/BAMS-83-11-1631>
- Li T (1997a) Air-sea interactions of relevance to the ITCZ: analysis of coupled instabilities and experiments in a hybrid coupled GCM. *J Atmos Sci* 54:134–147. [https://doi.org/10.1175/1520-0469\(1997\)054%3c0134:ASIORT%3e2.0.CO;2](https://doi.org/10.1175/1520-0469(1997)054%3c0134:ASIORT%3e2.0.CO;2)
- Li T (1997b) Phase transition of the El Niño-Southern oscillation: a stationary SST mode. *J Atmos Sci* 54:2872–2887. [https://doi.org/10.1175/1520-0469\(1997\)054%3c2872:PTOTEN%3e2.0.CO;2](https://doi.org/10.1175/1520-0469(1997)054%3c2872:PTOTEN%3e2.0.CO;2)
- Li T, Philander SGH (1996) On the annual cycle of the eastern equatorial Pacific. *J Clim* 9:2986–2998. [https://doi.org/10.1175/1520-0442\(1996\)009%3c2986:OTACOT%3e2.0.CO;2](https://doi.org/10.1175/1520-0442(1996)009%3c2986:OTACOT%3e2.0.CO;2)
- Lorenzo ED, Liguori G, Schneider N et al (2015) ENSO and meridional modes: A null hypothesis for Pacific climate variability. *Geophys Res Lett* 42:9440–9448. <https://doi.org/10.1002/2015GL066281>
- Martinez-Villalobos C, Vimont DJ (2016) The role of the mean state in meridional mode structure and growth. *J Clim* 29:3907–3921. <https://doi.org/10.1175/JCLI-D-15-0542.1>
- Martinez-Villalobos C, Vimont DJ (2017) An analytical framework for understanding tropical meridional modes. *J Climate* 30:3303–3323. <https://doi.org/10.1175/JCLI-D-16-0450.1>
- Pan X, Li T, Sun Y, Zhu Z (2021a) Cause of extreme heavy and persistent rainfall over yangtze river in summer 2020. *Adv Atmos Sci* 38:1994–2009. <https://doi.org/10.1007/s00376-021-0433-3>
- Pan X, Wang W, Li T et al (2021b) Cause of an extreme warm and rainy winter in Shanghai in 2019. *Int J Climatol* 41:4684–4697. <https://doi.org/10.1002/joc.7094>
- Park J-Y, Yeh S-W, Kug J-S, Yoon J (2013) Favorable connections between seasonal footprinting mechanism and El Niño. *Clim Dyn* 40:1169–1181. <https://doi.org/10.1007/s00382-012-1477-y>
- Philander SGH, Gu D, Lambert G et al (1996) Why the ITCZ is mostly north of the equator. *J Clim* 9:2958–2972. [https://doi.org/10.1175/1520-0442\(1996\)009%3c2958:WTIIMN%3e2.0.CO;2](https://doi.org/10.1175/1520-0442(1996)009%3c2958:WTIIMN%3e2.0.CO;2)
- Pickart RS, Macdonald AM, Moore GWK et al (2009) Seasonal evolution of aleutian low pressure systems: implications for the North Pacific subpolar circulation*. *J Phys Oceanogr* 39:1317–1339. <https://doi.org/10.1175/2008JPO3891.1>
- Rayner NA (2003) Global analyses of sea surface temperature, sea ice, and night marine air temperature since the late nineteenth century. *J Geophys Res* 108:4407. <https://doi.org/10.1029/2002JD002670>

- Richter I, Stuecker MF, Takahashi N, Schneider N (2022) Disentangling the North Pacific Meridional Mode from tropical Pacific variability. *NPJ Clim Atmos Sci* 5:1–9. <https://doi.org/10.1038/s41612-022-00317-8>
- Roeckner E, Arpe K, Bengtsson L, et al (1996) The atmospheric general circulation model ECHAM-4: Model description and simulation of present-day climate
- Rogers JC (1981) The North Pacific oscillation. *J Climatol* 1:39–57. <https://doi.org/10.1002/joc.3370010106>
- Saha S, Nadiga S, Thiaw C et al (2006) The NCEP climate forecast system. *J Clim* 19:3483–3517. <https://doi.org/10.1175/JCLI3812.1>
- Schneider U, Becker A, Finger P, et al (2015) GPCP monitoring product Version 5.0 at 1.0: Near Real-Time Monthly Land-Surface Precipitation from Rain-Gauges based on SYNOP and CLIMAT Data: Gridded Monthly Totals. 200 KB per monthly gzip file
- Stuecker MF (2018) Revisiting the Pacific meridional mode. *Sci Rep* 8:1–9. <https://doi.org/10.1038/s41598-018-21537-0>
- Vijith V, Vinayachandran PN, Webber BGM et al (2020) Closing the sea surface mixed layer temperature budget from in situ observations alone: Operation Advection during BoBBLE. *Sci Rep* 10:7062. <https://doi.org/10.1038/s41598-020-63320-0>
- Vimont DJ (2010) Transient growth of thermodynamically coupled variations in the Tropics under an Equatorially symmetric mean State*. *J Clim* 23:5771–5789. <https://doi.org/10.1175/2010JCLI3532.1>
- Vimont DJ, Wallace JM, Battisti DS (2003a) The seasonal footprinting mechanism in the Pacific: implications for ENSO. *J Clim* 16:8
- Vimont DJ, Wallace JM, Battisti DS (2003b) The Seasonal footprinting mechanism in the Pacific: implications for ENSO*. *J Climate* 16:2668–2675. [https://doi.org/10.1175/1520-0442\(2003\)016%3c2668:TSFMIT%3e2.0.CO;2](https://doi.org/10.1175/1520-0442(2003)016%3c2668:TSFMIT%3e2.0.CO;2)
- Vimont DJ, Alexander M, Fontaine A (2009) Midlatitude excitation of tropical variability in the Pacific: The role of thermodynamic coupling and seasonality*. *J Clim* 22:518–534. <https://doi.org/10.1175/2008JCLI2220.1>
- Wallace JM, Gutzler DS (1981) Teleconnections in the Geopotential Height Field during the Northern Hemisphere Winter. *Mon Wea Rev* 109:784–812. [https://doi.org/10.1175/1520-0493\(1981\)109%3c0784:TITGHF%3e2.0.CO;2](https://doi.org/10.1175/1520-0493(1981)109%3c0784:TITGHF%3e2.0.CO;2)
- Wang B, Wu R, Fu X (2000) Pacific-East asian teleconnection: How does ENSO affect East Asian Climate? *J Clim* 13:1517–1536. [https://doi.org/10.1175/1520-0442\(2000\)013%3c1517:PEATHD%3e2.0.CO;2](https://doi.org/10.1175/1520-0442(2000)013%3c1517:PEATHD%3e2.0.CO;2)
- Wang B, Wu R, Li T (2003) Atmosphere-Warm ocean interaction and its impacts on Asian-Australian Monsoon variation*. *J Climate* 16:1195–1211. [https://doi.org/10.1175/1520-0442\(2003\)16%3c1195:AOIAII%3e2.0.CO;2](https://doi.org/10.1175/1520-0442(2003)16%3c1195:AOIAII%3e2.0.CO;2)
- Wu S, Wu L, Liu Q, Xie S-P (2009) Development processes of the Tropical Pacific meridional mode. *Adv Atmos Sci* 27:95. <https://doi.org/10.1007/s00376-009-8067-x>
- Xiang B, Wang B, Li T (2013) A new paradigm for the predominance of standing Central Pacific Warming after the late 1990s. *Clim Dyn* 41:327–340. <https://doi.org/10.1007/s00382-012-1427-8>
- Xie S-P, Philander SGH (1994) A coupled ocean-atmosphere model of relevance to the ITCZ in the eastern Pacific. *Tellus a: Dynamic Meteorol Oceanography* 46:340–350. <https://doi.org/10.3402/tellusa.v46i4.15484>
- Yeh S-W, Kirtman BP (2004) The North Pacific Oscillation–ENSO and internal atmospheric variability. *Geophys Res Lett.* <https://doi.org/10.1029/2004GL019983>
- Zebiak SE, Cane MA (1987) A model El Niño–Southern oscillation. *Mon Weather Rev* 115:2262–2278. [https://doi.org/10.1175/1520-0493\(1987\)115%3c2262:AMENO%3e2.0.CO;2](https://doi.org/10.1175/1520-0493(1987)115%3c2262:AMENO%3e2.0.CO;2)
- Zhang L, Chang P, Ji L (2009a) Linking the Pacific meridional mode to ENSO: coupled model analysis. *J Clim* 22:3488–3505. <https://doi.org/10.1175/2008JCLI2473.1>
- Zhang L, Chang P, Tippett MK (2009b) Linking the Pacific meridional mode to ENSO: utilization of a Noise filter. *J Clim* 22:905–922. <https://doi.org/10.1175/2008JCLI2474.1>
- Zhang H, Deser C, Clement A, Tomas R (2014) Equatorial signatures of the Pacific meridional modes: dependence on mean climate state: Zhang et al.: role of mean state in PMMs’ asymmetry. *Geophys Res Lett* 41:568–574. <https://doi.org/10.1002/2013GL058842>
- Zhang H, Clement A, Medeiros B (2016) The Meridional mode in an idealized aquaplanet model: dependence on the mean state. *J Clim* 29:2889–2905. <https://doi.org/10.1175/JCLI-D-15-0399.1>
- Zhang Y, Yu S, Amaya DJ et al (2021) Pacific meridional modes without equatorial Pacific influence. *Journal of Climate.* <https://doi.org/10.1175/JCLI-D-20-0573.1>
- Zhang Y, Yu S-Y, Amaya DJ et al (2022) Atmospheric forcing of the Pacific meridional mode: tropical Pacific-driven versus internal variability. *Geophys Res Lett.* <https://doi.org/10.1029/2022GL098148>
- Zheng Y, Chen W, Chen S et al (2021a) Asymmetric impact of the boreal spring Pacific Meridional Mode on the following winter El Niño–Southern Oscillation. *Int J Climatol* 41:3523–3538. <https://doi.org/10.1002/joc.7033>
- Zheng Y, Chen W, Chen S (2021) Intermodel spread in the impact of the springtime Pacific meridional mode on following-winter ENSO tied to simulation of the ITCZ in CMIP5/CMIP6. *Geophys Res Lett.* <https://doi.org/10.1029/2021GL093945>
- Zheng Y, Chen S, Chen W, Yu B (2023) A continuing increase of the impact of the spring North Pacific meridional mode on the following winter El Niño and Southern oscillation. *J Clim* 36:585–602. <https://doi.org/10.1175/JCLI-D-22-0190.1>
- Zhu Z, Li T, He J (2014) Out-of-phase relationship between Boreal Spring and summer decadal rainfall changes in Southern China*. *J Clim* 27:1083–1099. <https://doi.org/10.1175/JCLI-D-13-00180.1>

Publisher's Note Springer Nature remains neutral with regard to jurisdictional claims in published maps and institutional affiliations.

Springer Nature or its licensor (e.g. a society or other partner) holds exclusive rights to this article under a publishing agreement with the author(s) or other rightsholder(s); author self-archiving of the accepted manuscript version of this article is solely governed by the terms of such publishing agreement and applicable law.